CRYSTAL GROWTH & DESIGN

pubs.acs.org/crystal

Article

Epitaxial $ZnGeP_2$ Thin Films on Si and GaP by Reactive Combinatorial Sputtering in Phosphine

Rekha R. Schnepf,* M. Brooks Tellekamp, Theresa Saenz, John S. Mangum, Edwin Supple, Dennice M. Roberts, Craig L. Perkins, Karen N. Heinselman, Brian P. Gorman, Ann L. Greenaway, Eric S. Toberer, and Adele C. Tamboli

Cite This: *Cryst. Growth Des.* 2022, 22, 6131−6139

Read Online

ACCESS | Metrics & More | Article Recommendations | Supporting Information

ABSTRACT: Modern optoelectronic devices are constrained to a fixed collection of band gap and lattice parameter combinations by the limited number of semiconductors that can be epitaxially integrated with high crystal quality. II−IV−V_2 compounds are promising materials to break this paradigm as changes to the cation lattice site disorder can modify the band gap without a substantial change to the lattice parameter. $ZnGeP_2$ is a particularly interesting member of this group as it is lattice-matched to Si and GaP, but substantial work is needed to understand and improve the epitaxial growth of $ZnGeP_2$. In this paper, we report on the growth of epitaxial $ZnGeP_2$ on Si and GaP substrates via reactive combinatorial sputtering in phosphine gas. Reciprocal space maps revealed that films on both GaP and Si have high crystalline quality, matching that of the substrate. The out-of-plane lattice parameter was found to increase with increasing Ge content, displaying an alloy-like behavior. Films deposited on Si displayed a much larger range for the (004) peak full width at half maximum (FWHM) than those deposited on GaP. Due to the growth of a lower-symmetry material, $ZnGeP_2$, on a higher-symmetry substrate, Si, it is likely that the films grown on Si have antiphase domains and larger threading dislocation densities than those on GaP. Electron channeling contrast imaging revealed the films on GaP to be largely dislocation-free. In the films deposited on Si, the optical absorption onset energies trended toward lower energies with larger (004) FWHM values. These results suggest that the defects in the films on Si that result in a broadened (004) FWHM cause sub-band gap absorption. This work provides the first combinatorial study of epitaxial $ZnGeP_2$ on Si and GaP and demonstrates the strong potential for the growth of high-quality epitaxial $ZnGeP_2$ with future work optimizing synthesis conditions and substrate preparation.

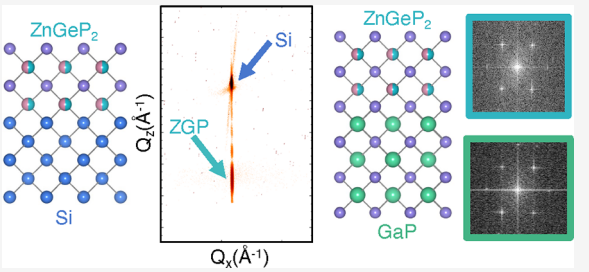

INTRODUCTION

There has been a growing interest in II−IV−V_2 materials due to the potential for tuning their properties, such as the band gap, at a fixed lattice parameter by utilizing site disorder.[1,2] While binary materials such as III−V's have proven to be very successful for optoelectronic device applications,[3,4] continued improvements are limited due to the narrow range of available band gaps for a given lattice constant when working with binary materials. Optoelectronic devices require high-quality interfaces and low defect densities, which means that an epitaxial alignment between layers is necessary. In order to maintain the epitaxy and reach the desired band gaps for layers in a III−V device, complex and expensive growth methods are needed.[5,6] Integrating aliovalent ternary materials, such as II−IV−V_2 materials, into devices could address some of the issues facing III−V materials by broadening the available band gaps for a given lattice constant.[1,2] II−IV−V_2 compounds have separately been identified as candidate materials for photovoltaic and photocatalytic applications.[7,8] However, the ability to grow high-quality epitaxial material will be necessary in order to realize the potential of II−IV−V_2 materials for devices.

$ZnGeP_2$ is a particularly compelling II−IV−V_2 material because it is lattice-matched to Si and GaP. It can form in either a cation-ordered chalcopyrite structure or a cation-disordered zinc blende structure. Similar to other II−IV−V_2 materials, it is predicted that its band gap can be decreased while maintaining a virtually unchanged *a* lattice parameter by increasing cation site disorder. This phenomenon has been experimentally demonstrated as a decrease in absorption onset energy with increasing disorder.[9] The ability to change the band gap while maintaining the lattice match to silicon makes $ZnGeP_2$ a promising candidate for a top cell absorber on a silicon tandem photovoltaic or photoelectrochemical device.[10]

Received: June 27, 2022
Revised: August 24, 2022
Published: September 6, 2022

https://doi.org/10.1021/acs.cgd.2c00723
Cryst. Growth Des. 2022, 22, 6131−6139

Additionally, the lattice match to GaP and the potential for tunable properties could enable $ZnGeP_2$ to be suitable as a cladding layer or a visible spectrum emitter for light-emitting diodes (LEDs).[1] The first step in exploring either of these device applications will be to grow high-quality epitaxial $ZnGeP_2$ on Si and GaP.

The existing literature on thin film synthesis of $ZnGeP_2$ is limited, with a few recent reports of polycrystalline thin films[9,11,12] and only two papers from the late 1980s and early 90s on epitaxial growth.[13,14] In the work conducted by Xing, et al., epitaxial $ZnGeP_2$ on GaP and Si substrates were synthesized via metalorganic vapor-phase epitaxy (MOVPE). They observed changes in the lattice constant and cation ordering in the $ZnGeP_2$ films as a function of the film composition.[13,14] Similar chalcopyrite and zinc blende II−IV−V_2 materials, such as $ZnSiP_2$, $ZnSnP_2$, $ZnSnAs_2$, $CdSnP_2$, and $MgGeAs_2$, have been synthesized by means of molecular beam epitaxy (MBE),[15−17] liquid-phase epitaxy (LPE),[18,19] low-pressure chemical vapor deposition with a combination of hydride and elemental precursors,[20] and vapor−liquid−solid growth.[21] The use of sputtering for the synthesis of epitaxial II−IV−P_2 materials has not yet been explored but has been utilized to grow polycrystalline $ZnGeP_2$ films.[12] In the II−IV−N_2 space, combinatorial sputtering has been utilized to synthesize epitaxial $ZnGeN_2$[22] and $MgSnN_2$.[23] The use of a combinatorial approach in these studies allowed for an extended composition space to be explored, which in turn enabled a more robust understanding of the effects of the composition on epitaxial alignment and film quality.

In this work, we utilize reactive combinatorial sputtering in PH_3 gas to synthesize epitaxial $ZnGeP_2$ films across a range of compositions on Si and GaP substrates. The film compositions were determined by utilizing a combination of X-ray fluorescence (XRF), Rutherford backscattering (RBS) measurements, and Auger spectroscopy. The film quality and structure was analyzed through X-ray diffraction (XRD) measurements. The in-plane and out-of-plane lattice parameters were calculated by fitting the XRD data. The substrate−film interface and epitaxial quality of the film were imaged using transmission electron microscopy (TEM). Electron channeling contrast imaging (ECCI) was conducted to compare the film quality between the films deposited on GaP and Si. Finally, the absorption coefficient of the films was determined by modeling spectroscopic ellipsometry data where trends were identified between the optical absorption of the films and film quality.

METHODS

Growth Methods. Seven thin film sample libraries were deposited using a PVD Products sputter deposition system, as described in Ref. 12. The deposition system utilizes radio frequency co-sputtering of metallic targets, Zn and Ge, while flowing dilute phosphine, PH_3, gas (2% PH_3 in Ar) to deliver P to the chamber. The substrate heater and plasma formed during the sputter process are used to crack the PH_3 gas. Due to the toxicity of the PH_3 gas, particular steps were taken to ensure the safe operation of the deposition chamber, including monitoring of the lab air for PH_3 and the use of self-contained breathing apparatus when the chamber was vented. Details of safety measures that were in place can be found in Ref. 12. For this study, the Zn and Ge sources were 2″ metallic targets purchased from Kurt J. Lesker Company with 99.99 and 99.999% purity values, respectively. The Zn and Ge sputter guns were angled at 22° to the substrate normal. The substrate was not rotated during the deposition to allow for a gradient in Zn and Ge fluxes, and thus the composition, across the film. We refer to the resulting combinatorial thin film as a "sample library." All of the sample libraries reported in this work were deposited at an operating pressure of 7 mTorr with 28 sccm of the 2% PH_3 in an Ar gas mixture flowing into the chamber. Prior to these depositions, the chamber base pressure was approximately 7×10^{-7} Torr. The deposition rate for the films in this work ranged from 0.16 to 0.29 nm/min depending on growth conditions. Due to the different growth conditions and deposition rates, the sample libraries in this work range in thickness from 20 to 70 nm.

Two of the sample libraries were deposited on 2″ x 2″ p-type Si substrates purchased from International Wafer Service, Inc. The substrates were (100) oriented with a 6° offcut in the [111] direction. The substrates were cleaned using the standard Radio Corporation of America (RCA) cleaning techniques. To remove the oxide layer prior to growth, the substrates were soaked in a solution of 2% HF in deionized water for 3 min and then immediately loaded in the vacuum deposition system.

The other five sample libraries were deposited on 2″ diameter n-type GaP wafers purchased from MTI Corporation. The GaP wafers were (100) oriented with a 2° offcut toward the [101] direction. The back of the GaP wafers was coated with tantalum to create a similar heating profile to that of the Si substrates with the radiative heater in the deposition chamber. Prior to a deposition, the GaP wafers were soaked in acetone, isopropanol, and deionized water for 2 min each. The wafers were then either baked on a hot plate at 100 °C for 10 min or held under vacuum in the deposition chamber load lock overnight to ensure that any solvent residue had evaporated. Finally, to remove the oxide layer, the GaP substrates were then soaked in a 15:1:1 H_2SO_4:H_2O_2:H_2O (piranha) solution for 60 seconds. After the piranha solution treatment, the GaP substrate was immediately loaded in the vacuum chamber. The piranha pretreatment of GaP substrates has previously been described in Ref. 24.

Characterization Methods. Films were characterized using a suite of spatially resolved characterization tools available at the National Renewable Energy Laboratory. These tools collect measurements using a standardized 4 × 11 point grid, and this geometry is described in Ref. 25. However, because our samples only had a composition gradient across the 11 columns and did not have a temperature gradient down the four rows, we essentially only had 11 points per sample library. The COMBIgor data analysis package was utilized to process and analyze the mapping data.[26]

Film composition maps were collected using a Bruker M4 Tornado Micro-XRF spectrometer with a Rh excitation beam and two detectors. The XRF spectra were modeled to extract the film composition using the XMethods software package. For the samples deposited on Si, the XRF model was calibrated with RBS data to extract the relative atomic percents of Zn, Ge, and P. For the samples deposited on GaP, the XRF measurements were used to only determine the relative cation composition (Zn and Ge). Auger spectroscopy was conducted on one sample deposited on GaP to verify that the cation compositions matched the XRF. Additional RBS measurements were conducted to determine the phosphorous content in two of the films on GaP, as well as to verify that negligible amounts of oxygen were being incorporated. RBS was chosen as the method to calibrate the XRF because it is a quantitative composition technique that does not require a standard sample.

RBS was performed in a 168 degree backscattering geometry using a model 3S-MR10 system from National Electrostatics Corporation, with a 2 MeV He^+ beam. The film composition for the calibration was determined by building a model for the film/substrate stack and fitting elemental compositions using the RUMP analysis software.[27]

Structural characterization of the first row of the sample libraries was conducted using a Rigaku Smartlab X-ray diffractometer using Cu-Kα radiation with a Ge(220) x 2 monochromator. The Rigaku Smartlab was utilized to conduct $2\theta - \omega$ and ω (rocking curve) scans at each point with a beam slit size of 0.25 mm. The in-plane and out-of-plane lattice parameters were calculated by extracting the (004) and (113) peak positions from symmetric $2\theta - \omega$ scans. The peak positions were determined by fitting a Voigt function to each peak. A representative peak fit is shown in Figure 1a. Once the peak position

https://doi.org/10.1021/acs.cgd.2c00723
Cryst. Growth Des. 2022, 22, 6131−6139

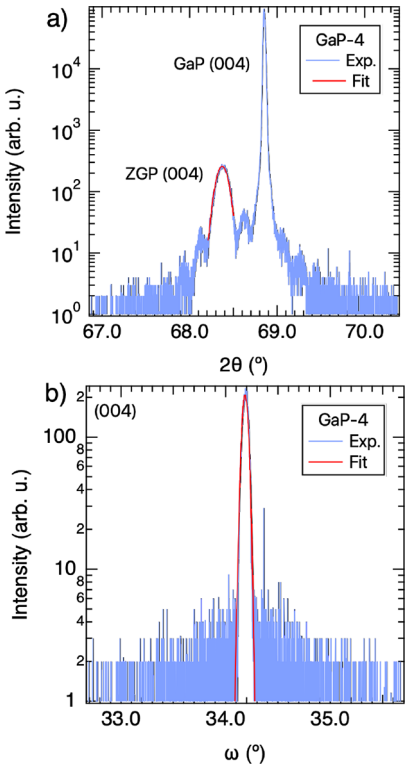

Figure 1. (a) Representative symmetric $2\theta-\omega$ scan with a Voigt fit utilized to determine the (004) peak position. (b) Representative rocking curve scan with the Pearson 7 fit used to extract the FWHM.

was determined, the corresponding d-spacing was calculated, and the lattice parameters were then calculated by a least-squares regression of the d spacing and the relationship for a tetragonal crystal structure and the lattice parameters. The error bars for the lattice parameters were calculated from the covariance matrix of the regression, taking into account the fitting error from the Voigt fit as an inverse weight. (004) full width at half maximum (FWHM) values were extracted from rocking curve measurements by fitting the data with a Pearson 7 fit function.

Reciprocal space maps (RSMs) were measured using a Panalytical MRD-Pro using Cu-Kα radiation monochromated using a four-bounce channel cut (400) Ge crystal and collimated using a Göbel mirror. The sample was positioned in an asymmetric geometry using a four-circle goniometer. A positive offset and a grazing-exit geometry were used to minimize the spot size on the combinatorial samples. The diffracted beam was collected using a 255 pixel × 255 pixel Si-CCD array with a step size of approximately 1/4 of the pixel-to-pixel spacing ($\sim 0.0025°$ 2θ).

TEM was conducted to image the substrate–film interface and verify the extent of epitaxy of three of the films. TEM lamellae were prepared using a ThermoFisher FEI Helios NanoLab 600i dualbeam focused ion beam scanning electron microscopy (FIB/SEM) instrument according to typical liftout methods.[28] A final 2 kV ion mill was used to minimize amorphous material on the lamella. Bright field, annular dark field, and high-angle annular dark field (HAADF) scanning transmission electron microscopy (STEM) images were recorded using a ThermoFisher FEI Talos F200X STEM instrument. Fast Fourier transforms (FFTs) of selected high-resolution STEM images were prepared using the FFT tool in ImageJ. ECCI was performed using a vCD backscatter detector inserted underneath the pole piece on an FEI Nova NanoSEM 630 operated at 25 kV accelerating voltage and 3.2 nA beam current. Channeling conditions were established by placing the electron beam axis at the intersection of the (220) and (040) band edges in the electron channeling pattern.

Spectroscopic ellipsometry was performed to determine the absorption coefficient of the samples. The measurements were conducted on the first row of each sample library using a J. A. Woollam Co. M-2000 variable angle ellipsometer at three angles: 65, 70, and 75°. These angles were chosen as they are close to the Brewster angle of Si, which is near 75°, in the wavelength range of the measurement. The CompleteEASE software (version 6.56) was used to create and fit optical models. The samples were modeled by fitting the imaginary part of the dielectric function with two Tauc–Lorentz oscillators.

RESULTS AND DISCUSSION

A variety of growth conditions were utilized to deposit $ZnGeP_2$ films over a range of compositions. A summary of the synthesis conditions is highlighted in Table 1. The first column of the table contains the sample IDs that will be used to identify the specific sample libraries throughout this paper. The corresponding experimental IDs that were used during the research can be found in Table S1 of the Supporting Information. The changes in growth conditions highlighted in Table 1 resulted in epitaxial $ZnGeP_2$ films over a spread of compositions. All of the sample libraries were deposited at temperatures of 400°C and above. Films deposited below 400°C were found to be polycrystalline. Figure 1 shows the representative XRD data for the films in this study, which are consistent with crystalline and highly-oriented epitaxial films. In Figure 1a, the $ZnGeP_2$ film (004) peak is identified next to the GaP (004) peak with thickness fringes visible surrounding the film peak. The representative rocking curve scan, shown in Figure 1b, reveals a sharp (004) peak, indicative of high crystalline quality. Figure 1a,b shows representative fit functions that were used to determine the lattice constants and (004) FWHM, respectively. 2D XRD detector images confirming that no other peaks or phases were detected can be found in Figure S2 of the Supporting Information. The range of cation compositions achieved across the films is illustrated in the ternary phase diagram in Figure 2a, which contains RBS-calibrated XRF data

Table 1. Various Growth Conditions That Correspond to Each Sample Library, along with the Sample IDs and Associated Data Symbols and Colors That Will Be Referenced throughout This Paper[a]

Sample ID	Temperature (°C)	Time (hrs)	Zn Power (W)	Ge Power (W)	Data Symbol
Si-1	400	5	80	6	▲
Si-2	400	4	90	8	▲
GaP-1	440	5	80	6	●
GaP-2	440	2.5	80	6	●
GaP-3	420	5	80	6	●
GaP-4	420	3.75	80	6	●
GaP-5	420	2.5	80	6	●

[a]The 5% PH_3 in Ar gas flow rate and growth pressure were held constant at 28 sccm and 7 mTorr, respectively, for all the depositions.

https://doi.org/10.1021/acs.cgd.2c00723
Cryst. Growth Des. 2022, 22, 6131–6139

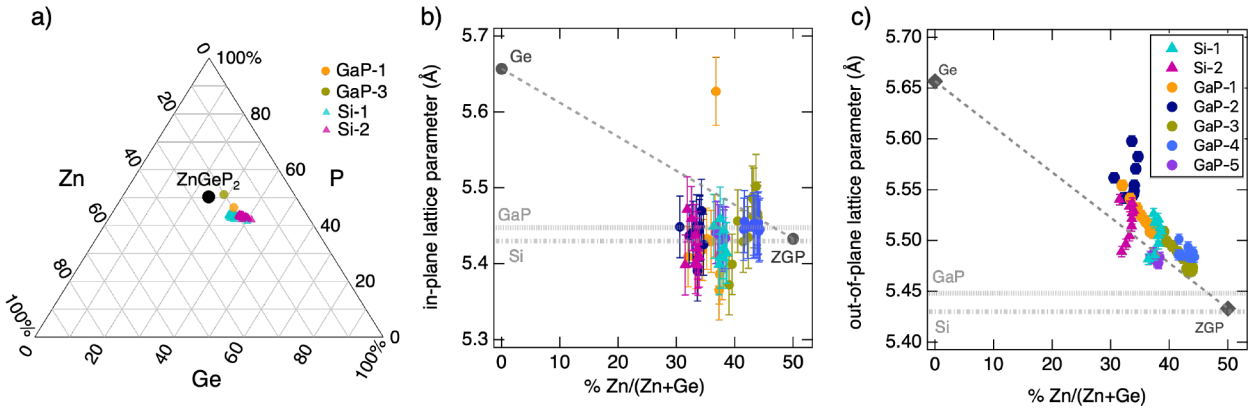

Figure 2. (a) Ternary diagram with the composition of the two sample libraries on silicon (from XRF) and two sample points from samples on GaP (from RBS). (b,c) In-plane lattice parameter and out-of-plane lattice parameter, respectively, for all seven sample libraries plotted vs % Zn on the cation site. The endpoints for cubic Ge[29] and cubic cation-disordered $ZnGeP_2$[30] are also included in each graph.

for the films on Si and RBS data for two sample points from films deposited on GaP. Due to the difficulty in accurately quantifying the P content in the films on GaP via XRF, RBS was necessary to determine the P content in these films. However, XRF could be used to measure the cation composition in the films on GaP. Auger spectroscopy was also conducted on one sample on GaP to verify that it agreed with the XRF and RBS results. The Auger spectroscopy results are included in Figure S1 of the Supporting Information. The RBS and Auger data measured the oxygen content at or below the noise level across all samples. In Figure 2a, it is shown that all of the films are Zn-poor, with less than the stoichiometric 25 at% of Zn. Additionally, only one sample that was measured, GaP-3, was found to have a stoichiometric amount of P. The elevated growth temperatures needed to synthesize epitaxial films combined with the high vapor pressure of Zn and P is likely the reason why most of the films are Zn- and P-poor.

Further analysis of the composition data exposes the sensitivity of phosphorous incorporation to changes in temperature. Both RBS and Auger spectroscopy found the phosphorous content in GaP-1, deposited at 440°C, to be around 45 at%. However, in sample library GaP-3, which was deposited at the slightly lower temperature of 420°C, a higher phosphorous content of 51 at% was determined by RBS. This finding suggests that for the samples on the GaP substrates, the increase in temperature from 420 to 440°C results in significant P desorption. Finally, in the samples on Si, both deposited at 400°C, we observe little change in the P content despite some changes in target powers. This suggests that temperature plays a leading role in the P incorporation in the films. Overall, these results highlight the challenge in growing epitaxial $ZnGeP_2$ films, where high temperatures are necessary for epitaxy but also cause difficulties in maintaining stoichiometric compositions.

Figure 2b,c shows the lattice parameter data for the first row of all the sample libraries plotted against the percent of Zn on the cation sites, % Zn/(Zn + Ge). The in-plane and out-of-plane lattice parameters were calculated from the (004) and (113) peak positions from symmetric $2\theta - \omega$ scans. A representative (004) peak fit is shown in Figure 1a. Figure 2b reveals that there is limited spread in the in-plane lattice constant across the samples and no trend with the cation composition. The vast majority of the samples have in-plane lattice constants within the error of the expected value for disordered $ZnGeP_2$ and the Si or GaP substrates.

The lack of a trend in the in-plane lattice parameter contrasts with the results for the out-of-plane lattice parameter. In Figure 2c, we observe a clear trend of an increasing out-of-plane lattice parameter with decreased Zn content (increased Ge content). The out-of-plane lattice parameter data roughly follows a linear trend between the disordered $ZnGeP_2$ lattice parameter and the lattice parameter for cubic Ge. The expanding out-of-plane lattice parameter to accommodate additional Ge in the crystal structure, while the in-plane lattice parameter remains close to the substrate lattice parameter, suggests an alloy-like behavior in films that are strained to the substrate.

TEM images were collected on samples and confirmed the epitaxial nature of the films. The substrate−film interface for GaP-4 is shown in Figure 3. FFTs were calculated from the highlighted regions in Figure 3 and show matching crystalline patterns for the substrate and film. TEM was also conducted on Si-1 and GaP-1, which also showed an epitaxial alignment at the substrate−film interface. However, these films were damaged by the high-kilovolt ion beam during FIB lift out of

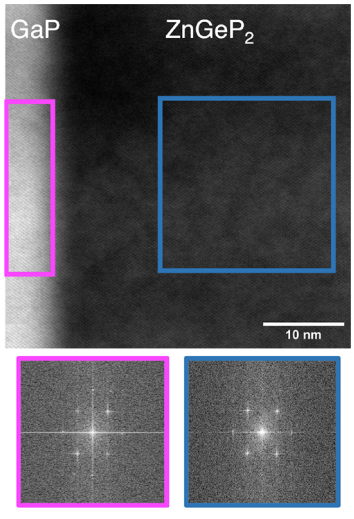

Figure 3. STEM bright field image of the substrate−film interface for sample GaP-4. FFTs of the indicated regions on the GaP substrate and $ZnGeP_2$ film show matching single crystal patterns.

https://doi.org/10.1021/acs.cgd.2c00723
Cryst. Growth Des. 2022, 22, 6131−6139

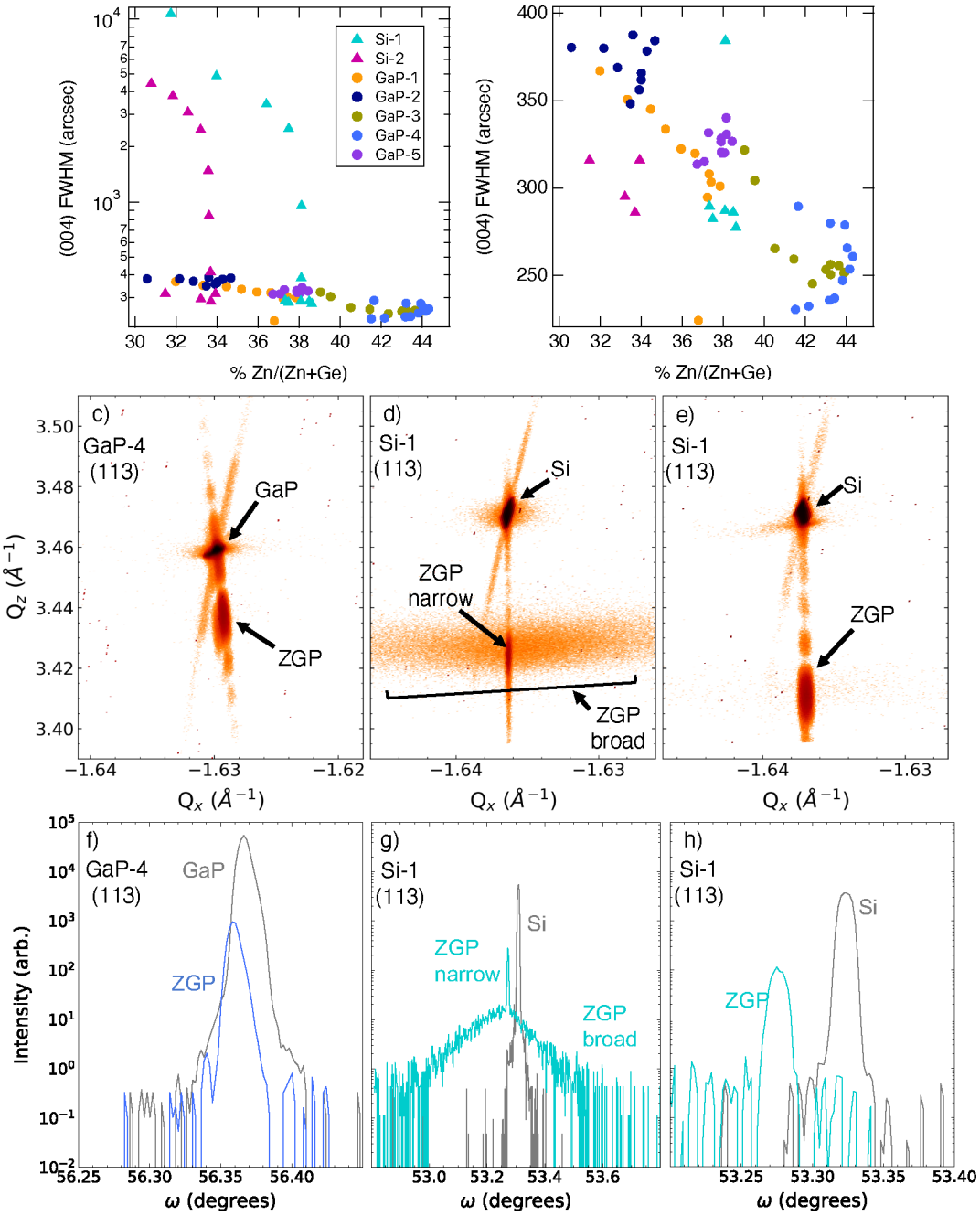

Figure 4. (a) (004) peak FWHM for all seven sample libraries plotted on a log scale with %Zn/(Zn + Ge) on the x-axis. (b) (004) peak FWHM plotted with the y-axis constrained to highlight the trend in the lower FWHM values with the cation composition. Representative RSMs for the films deposited on (c) GaP, (d) Si with the (004) FWHM values of 1000 arcsec and above, and (e) Si with the (004) FWHM values below 400 arcsec. (f–h) ω scans extracted from the RSMs. (f) and (h) are plotted with the same x-axis intervals because these peaks have similar FWHM values. However, (g) is plotted with a larger *x*-axis interval to accommodate the broadness of the film (113) peak.

TEM specimens, resulting in the top portion of the films becoming amorphous. To avoid damaging GaP-4 during the FIB lift out process, we added a protective layer to the top of the film, simply by drawing on the film using a permanent marker. We found that the permanent maker protected the surface of the sample enough to prevent the amorphization. The preparation method with a permanent marker was utilized for the film shown in Figure 3. Additional TEM images for the films that were damaged during the TEM preparation but still display an epitaxial alignment at the substrate–film interface are shown in Figure S5 of the Supporting Information.

Rocking curve measurements of the (004) peak were fit to extract FWHM data across all sample libraries, and these results support the conclusion that high-quality epitaxial $ZnGeP_2$ was achieved on both GaP and Si. A representative example of the (004) rocking curve peak fit is shown in Figure 1b. A summary of all the FWHM data is shown in Figure 4a. All of the GaP samples have an (004) FWHM below 400 arcsec. Many of the sample points on Si also have an (004) FWHM below 400 arcsec; however, there are several points with significantly larger values. These results suggest that there is more variability in film quality across the sample libraries on

https://doi.org/10.1021/acs.cgd.2c00723
Cryst. Growth Des. 2022, 22, 6131–6139

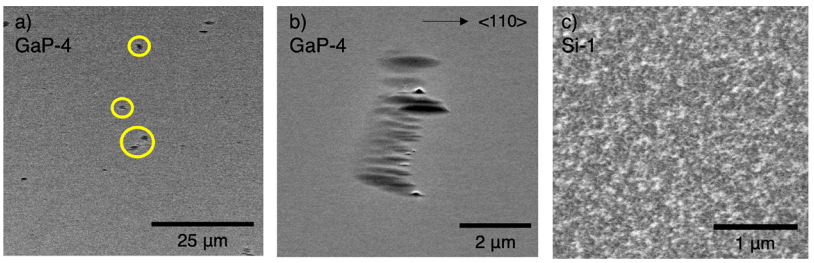

Figure 5. (a) Large-area ECCI micrograph of GaP-4 with some strain features, a few of which have been circled. (b) Representative zoomed-in ECCI micrograph of one of the strain features. (c) ECCI micrograph of Si-1 displaying surface roughness. For all ECCI micrographs, the detector was directly above the sample and the sample was tilted only a few degrees from the normal.

Si. A plot with a constrained range for the FWHM, to zoom in on the sample points with the smaller FWHM values, is shown in Figure 4b. In the constrained FWHM range, the samples roughly follow a trend of decreasing FWHM as the Zn content becomes closer to stoichiometric. The increased Ge content could result in an increased FWHM due to the larger lattice parameter of Ge, causing more misfit dislocations. Overall, the FWHM results indicate that a high-quality material was achieved on both substrates, though more consistently on GaP. One form of defects that may contribute to the larger FWHM in the films on Si are antiphase domains. Antiphase domains are defects that commonly occur when growing a lower-symmetry material on a higher-symmetry substrate, referred to as polar-on-nonpolar growth, and can result in high threading dislocation densities.[31−33] When growing disordered $ZnGeP_2$ on GaP, such as the films in this work, both the film and substrate have matching symmetry with the zinc blende structure, and there should not be significant antiphase domain formation. However, it should be noted that in the growth of cation-ordered chalcopyrite $ZnGeP_2$ on GaP, antiphase domains could form in the cation sublattice of the $ZnGeP_2$. In III−V heterostructures on Si, it has been found that depositing a GaP layer on Si and then depositing the other III−V layers can eliminate issues related to the epitaxial growth of a lower-symmetry material on a higher-symmetry material in the active material.[31] The extensive work done on the development of defect-free GaP on Si has proven the ability to suppress the formation of antiphase boundaries and other heterovalent nucleation-related defects.[31,34−37] It is possible that exploring this approach for future epitaxial $ZnGeP_2$ growth on Si could help reduce defect concentrations and increase material quality.

Reciprocal space maps (RSMs) of the (113) planes, shown in Figure 4c−e, reveal that while the sample libraries on Si have a larger variation in film quality, sample library points on both GaP and Si have film quality matching that of the substrate. Both for the samples on GaP, shown in Figure 4c, and on Si, shown in Figure 4d,e, the substrate and film (113) peaks are aligned in Q_x, indicating that the epilayers are strained in-plane to the substrate. The RSM for the sample on GaP, shown in Figure 4c, reveals a very narrow (113) peak, with an FWHM of 28.5 ± 0.2 arcsec, matching the width of the substrate peak, which has an FWHM of 29.6 ± 0.2 arcsec. The ω scan extracted from the RSM that was used to determine the FWHM is shown in Figure 4f. The similar FWHM values for the (113) peak in the GaP substrate and $ZnGeP_2$ film suggests that the film is of similar quality to the substrate and has low dislocation densities. For the sample on Si with an (004) peak FWHM value over 1000 arcsec, there is a sharp (113) peak with significant broadening in Q_x around it, and these features are labeled in Figure 4d,g. The FWHM associated with the narrow peak is 16.2 ± 0.1 arcsec, and the FWHM associated with broad peak is 690.5 ± 11.7 arcsec. The overlaying features of a narrow peak and a broad peak are indicative of this sample point having both regions with low dislocation densities and areas with disturbances in the lateral coherence of the films, such as dislocations, antiphase domains, or tilted grains. In the work conducted on sputtered epitaxial AlN films on sapphire, a similar overlay of a sharp peak and a broad peak was found in their ω scans, which was attributed to the relaxation in the film after a critical thickness resulting in a two-layer structure.[38] One layer was perfectly aligned to the substrate and the other layer contained tilt and twist components that resulted in the broader XRD peak. It is possible that relaxation due to increased thickness is causing some of the peak broadening shown in Figure 4d. In sample library Si-1, there is an 18 nm range in thicknesses, as determined by ellipsometry. If the thickness range in these samples is straddling the critical thickness, then this could explain why there is a range in FWHM values across the Si sample libraries. In Figure S6 of the Supporting Information, it can be seen that the (004) FWHM values for the two samples on Si do increase after the films are more than 55 nm thick. However, we cannot attribute the variability in film quality on Si substrates to thickness with full certainty. Additional factors, such as the changing composition across the sample libraries and insufficient substrate preparation enabling APDs in regions of the film, could have also caused the inconsistent film quality in the samples on Si. The variable quality in the films on Si is highlighted by comparing Figure 4d with Figure 4e, which shows the RSM for the (113) peak for a sample point with an (004) FWHM of less than 300 arcsec. The corresponding ω scan for the high quality point on silicon is shown in Figure 4h, and the FWHM of the film (113) peak, 36.3 ± 0.7 arcsec, nearly matches that of the substrate, 32.2 ± 0.6 arcsec. It should be noted that the FWHM values for the (113) peaks extracted from the RSMs are significantly smaller than those determined for the (004) peaks from the rocking curve measurements in Figure 4a,b. The broadening in the (004) peaks is due to the geometry and optics used for those measurements, which were needed for combinatorial mapping. While the exact FWHM values in Figure 4a,b contain some instrumental broadening and cannot be quantitatively compared to the RSM data, the experiments were controlled in a self-consistent manner and the trends within those data sets are valid. Overall, the RSM results show the ability to grow high-quality films on GaP and Si, with samples on each substrate showing film quality that matches that of the substrate.

https://doi.org/10.1021/acs.cgd.2c00723
Cryst. Growth Des. 2022, 22, 6131−6139

ECCI data qualitatively support the conclusion that the samples on GaP are of generally higher crystalline quality than those on Si. An ECCI micrograph of the GaP-4 surface is shown in Figure 5a and reveals the sample to be largely defect-free with some sparsely scattered clusters of strain inhomogeneity. Figure 5b shows a representative zoomed-in ECCI micrograph of one of the GaP-4 strain features, which routinely include dark triangular features and larger oval-shaped regions that exhibit neighboring areas of dark and bright contrast. These contrast variations in ECCI likely reveal regions of local strain inhomogeneities in the film. Similar oval-shaped features have been observed in III−V films grown by MBE, which were attributed to contamination on the substrate surface or impurities from elemental sources that result in localized inhomogeneous growth and strain.[39,40] The random arrangement of the oval-shaped features revealed by ECCI in the $ZnGeP_2$ films grown on GaP suggests that their origin is linked to extrinsic factors such as contamination left on the substrate surface or impurities introduced during the sputtering process. In Ref. 39, they attribute the surface contaminants to the residual sulfur left on the surface after etching the substrate in a 4:1:1 H_2SO_4:H_2O_2:H_2O solution prior to the film growth. A 15:1:1 H_2SO_4:H_2O_2:H_2O solution was used for this work, so it is possible that some of the contaminants here are also residual sulfur on the substrate surface. Unfortunately, the surface of the sample grown on Si, corresponding to a point on the film with an (004) FWHM below 300 arcsec, appears too rough to conclusively detect any defects by ECCI, as shown in Figure 5c. An SEM image of Si-1 shows similar surface roughness and is included in Figure S8 of the Supporting Information These results qualitatively agree with the (004) FWHM and (113) RSM results, which suggested that the films on GaP are generally of higher quality than the films on Si.

Representative optical absorption coefficient data for the sample libraries included in this paper are shown in Figure 6 and are generally consistent with previous data on Ge-rich disordered $ZnGeP_2$[12] but are also suggestive of trends in the absorption coefficient with film quality. Representative absorption coefficient data for the sample libraries on GaP and Si are shown in Figure 6a,b, respectively, with trace color representing the %Zn/(Zn + Ge). All of the samples have an absorption onset energy of around 1 eV, significantly lower than the 2.2 eV calculated band gap for ordered $ZnGeP_2$,[41] which is consistent with the expected narrowing of the band gap for cation-disordered $ZnGeP_2$.[9] It is also possible that the excess Ge in the films contributed to a reduction in the band gap as Ge has a narrower band gap of 0.66 eV. However, while the absorption onset energy trends to lower values with excess Ge content for the samples on Si, it remains fairly constant for the sample on GaP despite a similar composition range in both films. As described earlier, the range in film quality, quantified as the (004) FWHM, is varied between these two libraries. The sample on Si displayed a much larger range in FWHM values than the sample on GaP, as shown in Figure 4a. To highlight the effects of the (004) FWHM on the absorption onset energy, we have plotted the absorption threshold energy versus the (004) FWHM in Figure 6c. The absorption threshold energy is the energy value at which the absorption coefficient reaches a value of 10^4 cm^{-3}. In Figure 6c, we observe that in Si-1 and GaP-1, which span a similar range of cation compositions, the GaP library has both a narrow range of (004) FWHM values and absorption threshold values. In Si-1,

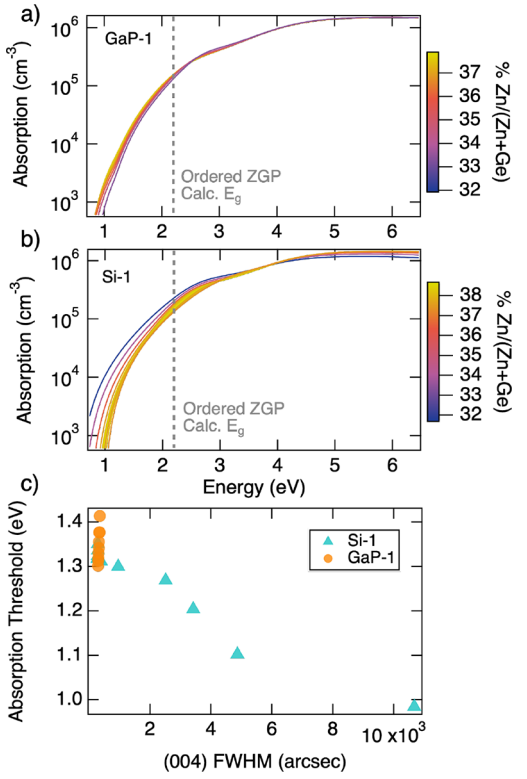

Figure 6. Representative absorption coefficient data for the sample on GaP (a) and Si (b) plotted with a color scale corresponding to the % Zn on the cation sites. (c) Absorption threshold energy plotted vs the (004) FWHM values. The absorption threshold energy is the energy at which the absorption coefficient reaches a value of 10^4 cm^{-3}.

which has a much broader range in (004) FWHM values, we see a trend of decreased absorption threshold energy with increased (004) FWHM. These results suggest that the crystalline quality, quantified by the (004) FWHM, affects the optical absorption properties. It is possible that with lower crystalline quality and increased FWHM, there are more defects causing sub-band gap absorption, resulting in a lower absorption onset energy. We can attribute the spread in absorption onset energies in the Si samples to defects rather than alloying with Ge because we do not see the same shifts in the absorption coefficient in the samples on GaP, which also have varied Zn and Ge contents but a smaller range in the FWHM.

CONCLUSIONS

In this paper, we have presented the growth of epitaxial cation disordered $ZnGeP_2$ on GaP and Si. Reactive combinatorial co-sputtering in PH_3 gas was utilized to grow the films over a range of compositions. TEM and XRD confirmed the epitaxial nature of the films. RSMs revealed the films to be strained to the substrate and found that high-quality material was achieved on both the GaP and Si substrates. Calculations of the out-of-plane lattice parameters suggest an alloy-like behavior with the out-of-plane lattice parameter increasing with increasing Ge content. Additionally, the (004) peak FWHM was also found to increase with increasing Ge content, suggesting that excess Ge results in increased defects in the films. A much larger range in the (004) FWHM was found for the samples on Si, indicating a larger variability in film quality for the films on Si. ECCI also qualitatively supported the conclusion that the

https://doi.org/10.1021/acs.cgd.2c00723
Cryst. Growth Des. 2022, 22, 6131−6139

$ZnGeP_2$ films deposited on GaP are of higher quality than those deposited on Si. The decreased quality in the films deposited on Si is likely a result of increased antiphase boundaries and dislocations arising from depositing a lower-symmetry material on a higher-symmetry material. Finally, the optical absorption onset energy for all films was found to be around 1 eV. However, the samples on Si exhibited a larger range of absorption onset energies, which was found to trend to lower energies with the increasing (004) FWHM. The absorption results indicate that the additional defects that are contributing to the larger FWHM values in the samples on Si could be causing sub-band gap absorption. This work provides the first combinatorial study of the epitaxial growth of $ZnGeP_2$ on Si and GaP. This confirms the ability to grow an epitaxial material on both substrates over a range of cation compositions with optical properties varying as a function of film quality, a critical step toward the integration of $ZnGeP_2$ and other II−IV−V_2 compounds as device layers. Future work to improve the quality of the films on Si might include growth on Si substrates with a GaP layer to minimize possible challenges arising from the symmetry difference between the film and substrate.

■ ASSOCIATED CONTENT

Supporting Information

The Supporting Information is available free of charge at https://pubs.acs.org/doi/10.1021/acs.cgd.2c00723.

Additional characterization data including Auger spectroscopy, XRD, TEM, SEM, and atomic force microscopy (PDF)

■ AUTHOR INFORMATION

Corresponding Author

Rekha R. Schnepf − *Physics Department, Colorado School of Mines, Golden, Colorado 80401, United States; National Renewable Energy Laboratory, Golden, Colorado 80401, United States;* orcid.org/0000-0002-3266-8916; Email: rschnepf.mines@gmail.com

Authors

M. Brooks Tellekamp − *National Renewable Energy Laboratory, Golden, Colorado 80401, United States;* orcid.org/0000-0003-3535-1831

Theresa Saenz − *Physics Department, Colorado School of Mines, Golden, Colorado 80401, United States; National Renewable Energy Laboratory, Golden, Colorado 80401, United States*

John S. Mangum − *National Renewable Energy Laboratory, Golden, Colorado 80401, United States;* orcid.org/0000-0002-5926-7565

Edwin Supple − *Metallurgical & Materials Engineering Department, Colorado School of Mines, Golden, Colorado 80401, United States*

Dennice M. Roberts − *National Renewable Energy Laboratory, Golden, Colorado 80401, United States;* orcid.org/0000-0003-0933-4587

Craig L. Perkins − *National Renewable Energy Laboratory, Golden, Colorado 80401, United States;* orcid.org/0000-0002-9036-8698

Karen N. Heinselman − *National Renewable Energy Laboratory, Golden, Colorado 80401, United States;* orcid.org/0000-0003-0287-3019

Brian P. Gorman − *Metallurgical & Materials Engineering Department, Colorado School of Mines, Golden, Colorado 80401, United States*

Ann L. Greenaway − *National Renewable Energy Laboratory, Golden, Colorado 80401, United States;* orcid.org/0000-0001-6681-9965

Eric S. Toberer − *Physics Department, Colorado School of Mines, Golden, Colorado 80401, United States*

Adele C. Tamboli − *National Renewable Energy Laboratory, Golden, Colorado 80401, United States; Physics Department, Colorado School of Mines, Golden, Colorado 80401, United States;* orcid.org/0000-0003-2839-9634

Complete contact information is available at: https://pubs.acs.org/10.1021/acs.cgd.2c00723

Notes

The authors declare no competing financial interest.

■ ACKNOWLEDGMENTS

The authors thank Bobby To for the atomic force microscopy and SEM data. The authors also thank Dr. Jacob Boyer for some helpful discussions. Primary funding was provided by the US. Department of Energy, Office of Science, Basic Energy Sciences, Materials Sciences and Engineering Division. The phosphide synthesis facility at the NREL is funded by the Liquid Sunlight Alliance, which is supported by the U.S. Department of Energy, Office of Science, Office of Basic Energy Sciences, Fuels from Sunlight Hub under Award Number DE-SC0021266. This work was authored in part by the National Renewable Energy Laboratory, operated by the Alliance for Sustainable Energy, LLC, for the US. Department of Energy (DOE) under Contract No. DE-AC36-08GO28308. The views expressed in the article do not necessarily represent the views of the DOE or the US. Government. The U.S. Government retains and the publisher, by accepting the article for publication, acknowledges that the U.S. Government retains a nonexclusive, paid-up, irrevocable, worldwide license to publish or reproduce the published form of this work, or allow others to do so, for U.S. Government purposes.

■ REFERENCES

(1) Schnepf, R. R.; Cordell, J. J.; Tellekamp, M. B.; Melamed, C. L.; Greenaway, A. L.; Mis, A.; Brennecka, G. L.; Christensen, S.; Tucker, G. J.; Toberer, E. S.; Lany, S.; Tamboli, A. C. Utilizing Site Disorder in the Development of New Energy-Relevant Semiconductors *ACS Energy Letters*; American Chemical Society, 2020; Vol. *5*, pp 2027−2041.

(2) Martinez, A. D.; Fioretti, A. N.; Toberer, E. S.; Tamboli, A. C. Synthesis, structure, and optoelectronic properties of II-IV-V2 materials. *J. Mater. Chem. A* **2017**, *5*, 11418−11435.

(3) Geisz, J. F.; France, R. M.; Schulte, K. L.; Steiner, M. A.; Norman, A. G.; Guthrey, H. L.; Young, M. R.; Song, T.; Moriarty, T. Six-junction III-V solar cells with 47.1% conversion efficiency under 143 Suns concentration. *Nature Energy* **2020**, *5*, 326−335.

(4) Pattison, M. Solid-State Lighting R&D Opportunities, 2019.

(5) Garcia, I.; France, R. M.; Geisz, J. F.; McMahon, W. E.; Steiner, M. A.; Johnston, S.; Friedman, D. J. Metamorphic III−V Solar Cells: Recent Progress and Potential. *IEEE Journal of Photovoltaics* **2016**, *6*, 366−373.

(6) Greenaway, A. L.; Boucher, J. W.; Oener, S. Z.; Funch, C. J.; Boettcher, S. W. Low-Cost Approaches to III−V Semiconductor Growth for Photovoltaic Applications. *ACS Energy Letters* **2017**, *2*, 2270−2282.

(7) Scanlon, D. O.; Walsh, A. Bandgap engineering of ZnSnP2 for high-efficiency solar cells. *Appl. Phys. Lett.* **2012**, *100*, 251911.
(8) Singh, A. K.; Montoya, J. H.; Gregoire, J. M.; Persson, K. A. Robust and synthesizable photocatalysts for CO2 reduction: a data-driven materials discovery. *Nat. Commun.* **2019**, *10*, 443.
(9) Schnepf, R. R.; Levy-Wendt, B. L.; Tellekamp, M. B.; Ortiz, B. R.; Melamed, C. L.; Schelhas, L. T.; Stone, K. H.; Toney, M. F.; Toberer, E. S.; Tamboli, A. C. Using resonant energy X-ray diffraction to extract chemical order parameters in ternary semiconductors. *J. Mater. Chem. C* **2020**, *8*, 4350−4356.
(10) Martinez, A. D.; Warren, E. L.; Gorai, P.; Borup, K. A.; Kuciauskas, D.; Dippo, P. C.; Ortiz, B. R.; Macaluso, R. T.; Nguyen, S. D.; Greenaway, A. L.; Boettcher, S. W.; Norman, A. G.; Stevanović, V.; Toberer, E. S.; Tamboli, A. C. Solar energy conversion properties and defect physics of ZnSiP2. *Energy Environ. Sci.* **2016**, *9*, 1031−1041.
(11) Schnepf, R. R.; Martinez, A. D.; Mangum, J. S.; Schelhas, L. T.; Toberer, E. S.; Tamboli, A. C. Disorder-tunable ZnGeP2 for epitaxial top cells on Si *IEEE 46th Photovoltaic Specialists Conference (PVSC)*; IEEE, 2019, pp 1052−1055.
(12) Schnepf, R. R.; Crovetto, A.; Gorai, P.; Park, A.; Holtz, M.; Heinselman, K. N.; Bauers, S. R.; Brooks Tellekamp, M.; Zakutayev, A.; Greenaway, A. L.; Toberer, E. S.; Tamboli, A. C. Reactive phosphine combinatorial co-sputtering of cation disordered ZnGeP2 films. *J. Mater. Chem. C* **2022**, *10*, 870−879.
(13) Xing, G.; Bachmann, K.; Solomon, G.; Posthill, J.; Timmons, M. Organometallic chemical vapor deposition of epitaxial ZnGeP2 films on (001) GaP substrates. *J. Cryst. Growth* **1989**, *94*, 381−386.
(14) Xing, G. C.; Bachmann, K. J.; Posthill, J. B.; Timmons, M. L. Substrate effects on the epitaxial growth of ZnGeP2 thin films by open tube organometallic chemical vapor deposition. *J. Appl. Phys.* **1991**, *69*, 4286−4291.
(15) St-Jean, P.; Seryogin, G. A.; Francoeur, S. Band gap of sphalerite and chalcopyrite phases of epitaxial ZnSnP2. *Appl. Phys. Lett.* **2010**, *96*, 231913.
(16) Li, Z.; Bender, H.; Malfait, M.; Moshchalkov, V. V.; Borghs, G.; Roy, W. V. MBE growth of MgGeAs2:Mn on GaAs substrate. *physica status solidi (a)* **2007**, *204*, 152−158.
(17) Asubar, J. T.; Jinbo, Y.; Uchitomi, N. MBE growth of Mn-doped ZnSnAs2 thin films. *J. Cryst. Growth* **2009**, *311*, 929−932.
(18) Zhang, L.; Zhang, G.; Cheng, K.; Zhang, P.; Liu, L.; Li, R.; Li, X.; Tao, X. Characterization of ZnSiP2 Films Grown on Si Substrate by Liquid Phase Epitaxy: Morphology, Composition, and Interface Microstructure. *Cryst. Growth Des.* **2019**, *19*, 3681−3687.
(19) Shay, J. L.; Bachman, K. J.; Buehler, E. Preparation and properties of CdSnP2/InP heterojunctions grown by LPE from Sn solution. *J. Appl. Phys.* **1974**, *45*, 1302−1310.
(20) Martinez, A. D.; Miller, E. M.; Norman, A. G.; Schnepf, R. R.; Leick, N.; Perkins, C.; Stradins, P.; Toberer, E. S.; Tamboli, A. C. Growth of amorphous and epitaxial ZnSiP2-Si alloys on Si. *J. Mater. Chem. C* **2018**, *6*, 2696−2703.
(21) Popov, V.; Pamplin, B. Epitaxial growth of solid solutions of ZnSiP2 in Si. *J. Cryst. Growth* **1972**, *15*, 129−132.
(22) Melamed, C. L.; Tellekamp, M. B.; Mangum, J. S.; Perkins, J. D.; Dippo, P.; Toberer, E. S.; Tamboli, A. C. Blue-green emission from epitaxial yet cation-disordered $ZnGeN2_{-x}O_x$. *Phys. Rev. Materials* **2019**, *3*, 051602.
(23) Greenaway, A. L.; Loutris, A.; Heinselman, K. N.; Melamed, C. L.; Schnepf, R. R.; Tellekamp, M. B.; Woods-Robinson, R.; Sherbondy, R.; Bardgett, D. J.; Bauers, S. R.; Zakutayev, A.; Christensen, S. T.; Lany, S.; Tamboli, A. Combinatorial synthesis of magnesium tin nitride semiconductors. *J. Am. Chem. Soc.* **2020**, *142*, 8421−8430.
(24) Mori, M. J.; Boles, S. T.; Fitzgerald, E. A. Comparison of compressive and tensile relaxed composition-graded GaAsP and (Al)InGaP substrates. *J. Vac. Sci. Technol., A* **2010**, *28*, 182−188.
(25) Fioretti, A. N.; Zakutayev, A.; Moutinho, H.; Melamed, C.; Perkins, J. D.; Norman, A. G.; Al-Jassim, M.; Toberer, E. S.; Tamboli, A. C. Combinatorial insights into doping control and transport properties of zinc tin nitride. *J. Mater. Chem. C* **2015**, *3*, 11017−11028.
(26) Talley, K. R.; Bauers, S. R.; Melamed, C. L.; Papac, M. C.; Heinselman, K. N.; Khan, I.; Roberts, D. M.; Jacobson, V.; Mis, A.; Brennecka, G. L.; Perkins, J. D.; Zakutayev, A. COMBIgor: Data-Analysis Package for Combinatorial Materials Science. *ACS Combinatorial Science* **2019**, *21*, 537−547.
(27) Barradas, N.; Arstila, K.; Battistig, G.; Bianconi, M.; Dytlewski, N.; Jeynes, C.; Kótai, E.; Lulli, G.; Mayer, M.; Rauhala, E.; Szilágyi, E.; Thompson, M. Summary of "IAEA intercomparison of IBA software. *Nucl. Instrum. Methods Phys. Res., Sect. B* **2008**, *266*, 1338−1342.
(28) Langford, R.; Rogers, M. In situ lift-out: Steps to improve yield and a comparison with other FIB TEM sample preparation techniques. *Micron* **2008**, *39*, 1325−1330.
(29) Cooper, A. S. Precise lattice constants of germanium, aluminum, gallium arsenide, uranium, sulphur, quartz and sapphire. *Acta Crystallographica* **1962**, *15*, 578−582.
(30) Vaipolin, A.; Osmanov, E.; Prochukhan, V. Modifications of A(II) B(IV) C2(V) compounds with the sphalerite structure. *Izvestiya Akademii Nauk SSSR,Neorganicheskie Materialy* **1972**, *8*, 947−949.
(31) Supplie, O.; Romanyuk, O.; Koppka, C.; Steidl, M.; Nägelein, A.; Paszuk, A.; Winterfeld, L.; Dobrich, A.; Kleinschmidt, P.; Runge, E.; Hannappel, T. Metalorganic vapor phase epitaxy of III-V-on-silicon: Experiment and theory. *Prog. Cryst. Growth Charact. Mater.* **2018**, *64*, 103−132.
(32) Kroemer, H. Polar-on-nonpolar epitaxy. *J. Cryst. Growth* **1987**, *81*, 193−204.
(33) Kvam, E. P. Interactions of dislocations and antiphase (inversion) domain boundaries in III-V/IV heteroepitaxy. *J. Electron. Mater.* **1994**, *23*, 1021−1026.
(34) Grassman, T. J.; Carlin, J. A.; Galiana, B.; Yang, L.-M.; Yang, F.; Mills, M. J.; Ringel, S. A. Nucleation-related defect-free GaP/Si(100) heteroepitaxy via metal-organic chemical vapor deposition. *Appl. Phys. Lett.* **2013**, *102*, 142102.
(35) Grassman, T. J.; Chmielewski, D. J.; Carnevale, S. D.; Carlin, J. A.; Ringel, S. A. $GaAs_{0.75}P_{0.25}$/Si Dual-Junction Solar Cells Grown by MBE and MOCVD. *IEEE Journal of Photovoltaics* **2016**, *6*, 326−331.
(36) Beyer, A.; Ohlmann, J.; Liebich, S.; Heim, H.; Witte, G.; Stolz, W.; Volz, K. GaP heteroepitaxy on Si(001): Correlation of Si-surface structure, GaP growth conditions, and Si-III/V interface structure. *J. Appl. Phys.* **2012**, *111*, 083534.
(37) Saenz, T. E.; McMahon, W. E.; Norman, A. G.; Perkins, C. L.; Zimmerman, J. D.; Warren, E. L.; *High-Temperature Nucleation of GaP on V-Grooved Si Crystal Growth & Design* American Chemical Society, 2020; Vol. *20*, pp 6745−6751.
(38) Miyake, H.; Lin, C.-H.; Tokoro, K.; Hiramatsu, K. Preparation of high-quality AlN on sapphire by high-temperature face-to-face annealing. *J. Cryst. Growth* **2016**, *456*, 155−159.
(39) Chai, Y. G.; Pao, Y.-C.; Hierl, T. Elimination of "pair" defects from GaAs layers grown by molecular beam epitaxy. *Appl. Phys. Lett.* **1985**, *47*, 1327−1329.
(40) Kakibayashi, H.; Nagata, F.; Katayama, Y.; Shiraki, Y. Structure Analysis of Oval Defect on Molecular Beam Epitaxial GaAs Layer by Cross-Sectional Transmission Electron Microscopy Observation. *Japanese Journal of Applied Physics* **1984**, *23*, L846−L848.
(41) High Performance Computing Center Materials Database. Materials.nrel.gov.

https://doi.org/10.1021/acs.cgd.2c00723
Cryst. Growth Des. 2022, 22, 6131−6139